Accepted Manuscript

Journal Name

Deciphering the Origin of the High Capacities Seen in Magnesium Borate Polyanion Cathodes

Camilla Tacconis,*[a] Sunita Dey[b,c], Carson D. McLaughlin[a], Debashis Tripathy[b], Heather F. Greer[b], Shaoliang Guan[a], Iuliia Mikulska[d], Israel Temprano[b], Clare P. Grey[b] and Siân E. Dutton[a]

Recent reviews have highlighted borate polyanion systems as promising high-voltage cathode candidates for rechargeable Mg-ion batteries (RMBs) [Coordination Chemistry Reviews, 427, 213551 (2021)]. However, evaluating the electrochemical performance of cathodes for Mg-ion batteries is challenging, with many reports relying on an observed electrochemical capacity rather than demonstrating Mg-ion (de)intercalation. To address these two points, we study three classes of borate polyanions: *orthoborates* $M_3(BO_3)_2$, *ludwigites* M_3BO_5, and *pyroborates* $M_2B_2O_5$ and use a suite of experimental techniques to investigate de-magnesiation on charging *vs* Li metal with a Li electrolyte. We select five representative materials $Mg_2Mn(BO_3)_2$, $Mg_2Ni(BO_3)_2$, Mg_2FeBO_5, $MgFeB_2O_5$ and $MgFe_{0.5}Mn_{0.5}B_2O_5$. Whilst promising first charge capacities up to 200 mAh g^{-1} are observed for ball-milled cathodes cycled at 55°C in a Li containing electrolyte, extensive post-cycling analysis using *ex-situ* X-ray Photoelectron Spectroscopy (XPS) and *ex-situ* Synchrotron Powder X-ray Diffraction (SXRD), combined with *operando* X-ray Absorption Spectroscopy (XAS) and *operando* Online Electrochemical Mass Spectrometry (OEMS), show that the capacities obtained are not associated with Mg^{2+} mobility in the cathodes, de-magnesiation or transition-metal redox. The observed capacity originates from a process enhanced by ball-milling, which is common to all borate polyanions investigated in this work. This process is in part attributed to the irreversible reaction of an amorphous surface layer on the polycrystalline particle, rich in carbonate and glassy borate phases. Here we present the first systematic study of the viability of transition-metal borate polyanions as intercalation cathode materials for RMBs and conclude that, despite the promising electrochemistry, these materials do not de-magnesiate under our tested conditions.

1 Introduction

The demand for batteries is rapidly increasing, whether to address the Battery Electric Vehicle (BEV) market, as a method to support the intermittency of renewable energy sources, or to power portable electronics[1–3]. Each battery application requires specific system characteristics, prioritising lower weight, high power or high energy density to different extents. Currently, lithium-ion batteries (LIBs) dominate the rechargeable battery market, but the sharp peak in lithium carbonate (Li_2CO_3) prices—over 350%

between 2017 and 2022[4,5]—has highlighted concerns about the scalability of LIB production, and the ability of Li resources to match the growing battery demands[6].

Given the diverse requirements for battery performance across their many applications, there is substantial scope for alternative battery technologies that do not rely on Li as the charge-transporting ion. There has been considerable research focus on next-generation rechargeable batteries, which may provide longer lifetimes, cost-effectiveness, sustainability, and the use of more abundant raw materials[7].

In this attempt to diversify the battery market, there is growing interest in multivalent batteries, which utilise ions transferring more than one electron per ion[8]. Among the most studied are magnesium (Mg^{2+}), zinc (Zn^{2+}), calcium (Ca^{2+}) and aluminium (Al^{3+}). Within these technologies, Mg ions hold the greatest promise, providing the second most competitive redox voltage - 2.37 V *vs* SHE[9,10], additionally being cheaper and more naturally abundant than lithium.

[a] *University of Cambridge, Department of Physics, JJ Thomson Ave, Cambridge, CB3 0HE, UK; e-mail: ct603@cam.ac.uk*

[b] *Yusuf Hamied Department of Chemistry, University of Cambridge, Lensfield Road, Cambridge, CB2 1EW, UK.*

[c] *University of Aberdeen, Advanced Centre for Energy and Sustainability (ACES), Department of Chemistry, AB24 3UE, UK.*

[d] *Diamond Light Source Ltd, Harwell Science & Innovation Campus, Didcot, Oxfordshire OX11 0DE, UK.*

† Supplementary Information available: [details of any supplementary information available should be included here]. See DOI: 00.0000/00000000.

The first rechargeable Mg-ion battery (RMB) capable of reversible Mg^{2+} intercalation was demonstrated in 2000 by Aurbach *et al.* employing the Chevrel phase Mo_6S_8 as the cathode material[11]. To date, Mo_6S_8 is the best-performing intercalation cathode for reversible Mg^{2+} storage, delivering a reversible capacity of 100 mAh g^{-1} over 2000 cycles in the range 0.5-2 V[12–14]. Despite this promising performance, the commercial viability of RMBs faces multiple challenges, including the lack of sufficiently high-voltage cathode materials and stable electrolytes compatible with high-voltage cathode candidates[15,16]. These issues must be addressed for RMBs to deliver commercially competitive energy densities and achieve commercial feasibility[17]. This study aims to investigate novel high-voltage cathode materials for RMBs.

1.1 Polyanion Cathode Materials

This work draws inspiration from the Li polyanion $LiFePO_4$[18], a cathode material experiencing increasing commercial success and gaining attention for its potential to enhance safety in future LIBs. The analogue Li borate polyanion $LiFeBO_3$ was first reported in 2000[19], demonstrating the extraction of only 0.04 Li, attributed to the material's low ionic and electronic conductivity. However, by 2010, Yamada *et al.* achieved full capacity by optimising synthesis methods, particle size, and morphology[20]. Lithium transition metal borates, $LiMBO_3$, have since attracted considerable attention for their high operating voltages (>4 V) and substantial capacities (>200 mAh g^{-1}), depending on the transition metal (TM) incorporated[21].

Building on the success of polyanions in Li battery technologies[22–24], here we explore magnesium borate polyanions as potential high-voltage cathode materials for RMBs. The polyanion inductive effect should offer high operating voltages while the low atomic mass of boron maximises gravimetric capacity[25,26]. We select materials formed with the borate BO_3^{3-} framework, which is the lightest polyanion group. Three distinct polyanion structures were investigated in this work: *orthoborates* $M_3(BO_3)_2$, *ludwigites* M_3BO_5, and *pyroborates* $M_2B_2O_5$. Table 1 summarises the key structural differences between the borates studied, which will be discussed in detail below. Here we adopt a useful notation to characterise polyanion compounds, where Δ is used to represent BO_3^{3-} trigonal planar units, which are the anionic borate groups used as building blocks for the polyanions in this study. These Δ units can coordinate individually to metal cations ($n = 0$), or form polymeric chains with adjacent Δ units by sharing n oxygen atoms ($n = 1 - 3$)[27].

1.1.1 Orthoborates $M_3(BO_3)_2$

Magnesium *orthoborates*, $Mg_2M(BO_3)_2$ (M = Ni, Mn), crystallise in the orthorhombic *Pnnm* space group, where the trigonal-planar $(BO_3)^{3-}$ units (Δ_0) form layered structures (Fig. S2). The unit cell is comprised of two distorted octahedral sites, $M1$ (blue) and $M2$ (pink), Fig. 1a, which are occupied by a disordered arrangement of magnesium and transition metal ions. Prior work used bond valence sum calculations to infer the presence of a feasible intercalation pathway for divalent ions[28]. While naturally occurring *orthoborates* were identified in the late 17th century, synthetic mixed-metal *orthoborates* were first reported in the late 20th century[29]. However, the use of *orthoborate* polyanions as potential cathode materials for magnesium-ion batteries to our knowledge has not yet been reported. In this study we evaluate two *orthoborate* systems $Mg_2Mn(BO_3)_2$ and $Mg_2Ni(BO_3)_2$, with theoretical capacities of 242.3 mAh g^{-1} and 238.3 mAh g^{-1}, respectively, corresponding to the removal of 1 Mg per formula unit and the oxidation of Mn/Ni from 2+ to 4+. A comparison of these theoretical capacities to the current benchmark set by Mo_6S_8, 129 mAh g^{-1}[30], positions *orthoborates* as promising cathode materials for RMBs.

1.1.2 Ludwigites M_3BO_5

Ludwigites, represented by the formula M_3BO_5, are a large family of materials named after the natural mineral ludwigite, Mg_2FeBO_5, containing $Fe^{2+/3+}$ and Mg^{2+} ions. *Ludwigite* materials typically contain a mixed-valence composition with $2M^{2+}$ and $1M^{3+}$ and present an orthorhombic unit cell with space group *Pbam*, illustrated in Fig. 1b. Zig-zag chains of edge-sharing MO_6 octahedra are connected by BO_3 trigonal planar units (Δ_0) and extend along the *c*-axis[31,32], Fig. S5. *Ludwigite* materials have four distinct metal sites, with disordered metal distribution across the four sites for hetero-metallic samples. A preferential occupation of sites $M3$ and $M4$ by divalent ions, with higher valence ions generally occupying sites $M1$ and/or $M2$, was observed by Perkins and Attfield[33].

While ludwigites have been studied for their magnetic properties[34], only one study explores their application as cathodes for Li-ion batteries, showing scarce ion intercalation at low redox potentials[35]. In this study, we focus on the mixed-metal system, Mg_2FeBO_5, as a candidate for magnesium-ion batteries. Mg_2FeBO_5 contains redox active Fe^{3+}, expected to undergo a redox transition of Fe from 3+ to 4+, yielding the theoretical capacity of 137.3 mAh g^{-1}.

Table 1 Summary of the borate structures studied in this work. Δ_n represents $(BO_3)^{3-}$ trigonal planar units, with the n subscript denoting the number of oxygens shared with other borate units. All the structures studied are characterised by a disordered occupation of Mg and the transition metals on the M sites. The theoretical capacities reported in this table are calculated differently for each material, dependent on the transition metal redox state reached during charge, the reader is referred to the main text in section 1.1 for a detailed discussion.

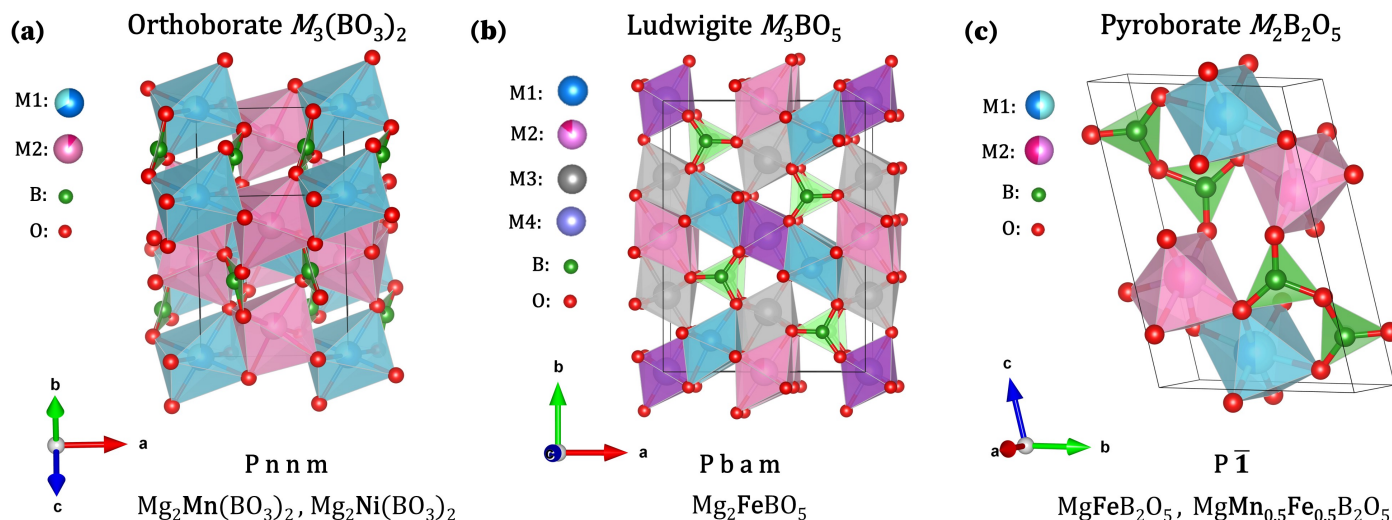| Borate Class	Composition	Borate Connectivity	Number of M sites	Transition metal Oxidation state	Compounds in this study	Theoretical Capacity (mAh g^{-1})
Orthoborate	$M_3(BO_3)_2$	Δ_0	2	2^+	$Mg_2Mn(BO_3)_2$ $Mg_2Ni(BO_3)_2$	242.3 238.3
Ludwigite	M_3BO_5	Δ_0	4	$2^+/3^+$	Mg_2FeBO_5	137.3
Pyroborate	$M_2B_2O_5$	Δ_1	2	2^+	$MgFeB_2O_5$ $MgFe_{0.5}Mn_{0.5}B_2O_5$	147.5 147.8

Fig. 1 Unit cells obtained from Rietveld refinement (SI Fig. S2-S3) for the borate polyanions investigated in this study: (a) *orthoborate* $M_3(BO_3)_2$, (b) *ludwigite* M_3BO_5, and (c) *pyroborate* $M_2B_2O_5$.

1.1.3 Pyroborates $M_2B_2O_5$

Pyroborates, with the general formula $M_2B_2O_5$, where M represents one or more divalent ions, exhibit two principal crystal structures: triclinic polymorph ($P\bar{1}$) and heteromorphous monoclinic ($P2_1/c$)[36,37]. The *pyroborates* synthesised in this study crystallised in the triclinic $P\bar{1}$ structure, characterised by 2D ribbons formed by four edge-sharing MO_6 octahedra extending along the *a*-axis, Fig. S4. These are linked together by the $B_2O_5^{4-}$ polyanion framework units, composed of two corner-sharing BO_3 triangles (Δ_1). A characteristic of the crystal structure is a 1:1 ratio of the distinct metal sites $M1$ (blue) and $M2$ (pink), with $M1$ being larger and more distorted and $M2$ having a larger bond angle variance, seen in Fig. 1c. Similarly to the other borates, these systems are characterised by a disordered occupation of the metals in the $M1$ and $M2$ sites.

A study from Strauss *et al.* studied pyroborate materials as cathodes for Li-ion batteries, showing limited electrochemical reactivity[38]. In a recent report from our group, Bo *et al.* were the first to explore the use of these materials in magnesium-ion batteries. Through bond valence sum maps, potential Mg^{2+} ionic diffusion pathways within the $Mg_xFe_{2-x}B_2O_5$ ($x = 2/3, 4/3$) *pyroborate* framework were identified, and detailed structural analysis used to show demagnesiation from the compounds at high temperatures obtained by thermogravimetric analysis[39]. Polyanion *pyroborates* $Mg_xMn_{2-x}B_2O_5$ ($x = 2/3, 4/3$) were studied as novel high-energy density cathodes for Li-ion batteries, with Mg removal demonstrated through minimal post cycling analysis[40]. A first study by our group on $MgFeB_2O_5$ demonstrated no electrochemical capacity from the cathode material, with the first charge capacity attributed to a Fe metal impurity deriving from synthesis[41]. In this study, we evaluate phase pure $MgFeB_2O_5$ and $MgFe_{0.5}Mn_{0.5}B_2O_5$ as a further possible class of Mg borate cathode materials. These materials are expected to yield theoretical capacities of 147.45 mAh g^{-1} and 147.8 mAh g^{-1}, respectively, as we primarily anticipate activating the 2+ to

3+ oxidation couple within the voltage range investigated in this work. This process would result in the removal of 0.5 Mg per formula unit. If the 2+ to 4+ redox transition were activated, the theoretical capacities could increase to 294.9 mAh g^{-1} and 295.6 mAh g^{-1}, leading to full de-magnesiation of the cathode materials.

1.1.4 Scope of this Study

The primary objective of this work was to evaluate the feasibility of Mg^{2+} removal from the host polyanion cathode structures. In this study, a wide range of polyanion materials were studied as Mg cathode materials for RMBs. Five different compositions from three polyanion groups were synthesised in phase pure form; $Mg_2M(BO_3)_2$ ($M=$ Ni, Mn), $MgMB_2O_5$ ($M=$ Fe, $Mn_{0.5}Fe_{0.5}$), and Mg_2FeBO_5, (Fig. S2-3). The possibility of Mg^{2+} deintercalation from these cathode structures was investigated through electrochemical studies and a wide range of post-cycling analysis techniques.

Among the key challenges for the commercial application of RMBs is the lack of stable Mg electrolytes compatible with oxygen-containing, high-voltage cathodes[42]. To address this issue, the cathode materials were tested in half cells using lithium metal as the reference electrode and LP30 electrolyte (1 M LiPF$_6$ in 50/50 v/v ethylene carbonate and dimethyl carbonate, EC/DMC), a system that is well-understood and electrochemically stable in the voltage ranges used for this study. The first charge behaviour of the cathodes was then investigated in depth to evaluate whether de-magnesiation had occurred from the cathode materials.

To our surprise, the trend observed in the borate polyanions studied in this work was similar for all the materials investigated. Therefore, we discuss $Mg_2Mn(BO_3)_2$ as a representative example, presenting a detailed post-cycling analysis of this system. We then identify possible mechanisms that could explain the similar behaviour of all the polyanions presented in this work. We
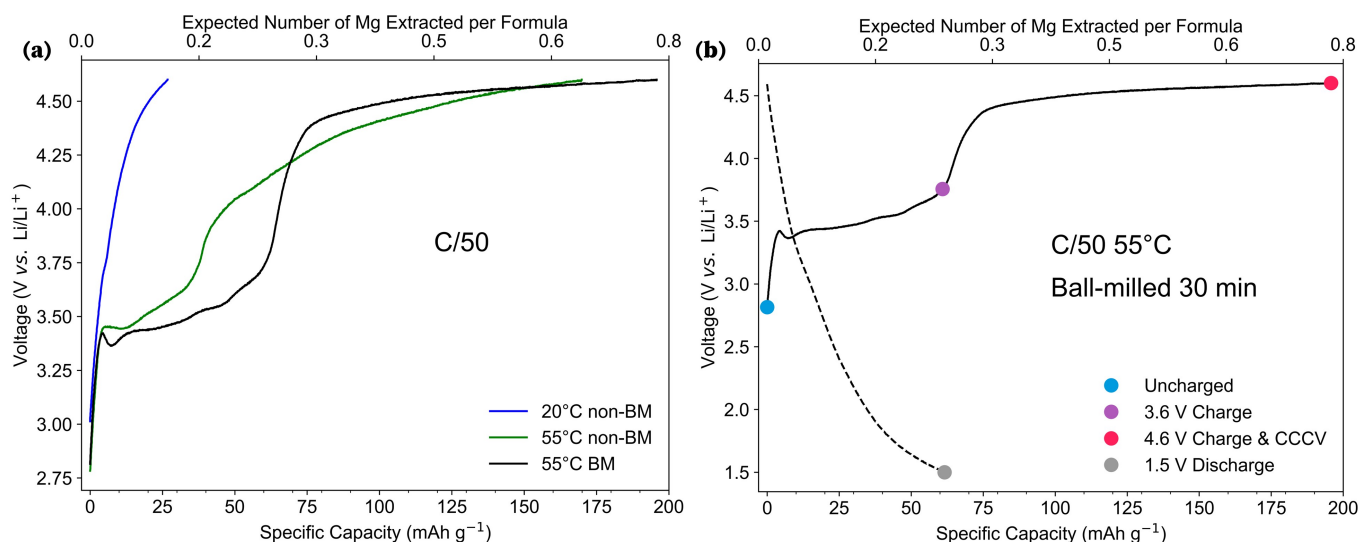
Fig. 2 (a) Comparison of the electrochemistry of $Mg_2Mn(BO_3)_2$ for different investigated temperatures and particle morphologies. (b) Electrochemistry of $Mg_2Mn(BO_3)_2$ charged to 4.6 V at a rate of C/50 in a 55°C, and held at 4.6 V until the current decayed to C/200, then discharged to 1.5 V. The number of moles of Mg extracted was calculated based on a theoretical capacity of 242.3 mAh g^{-1}. The coloured dots indicate the key points in the charge profile at which post-cycling analysis was performed.

hypothesise that the first charge irreversible capacity can be attributed to the irreversible reaction of an amorphous carbonate and borate glass surface layer on the cathode particles. Insights into the performance of the multiple borate polyanions as cathode materials for RMBs are derived through these comprehensive experimental studies.

2 $Mg_2Mn(BO_3)_2$ Case Study

2.1 Evaluation of Electrochemical Behaviour

The theoretical capacity of $Mg_2Mn(BO_3)_2$ was calculated to be 242.3 mAh g^{-1}, corresponding to the removal of one Mg ion per formula unit, accompanied by a $Mn^{2+} \rightarrow Mn^{4+}$ redox process. Initial electrochemical testing, performed in coin cells at room temperature, yielded capacities of approximately 27 mAh g^{-1} during the first charge, seen in blue in Fig. 2a. To improve Mg-ion diffusion, the cells were cycled at an elevated temperature of 55°C. This is common practice in Mg-ion battery research due to the sluggish (de)intercalation of Mg^{2+} ions at room temperature, caused by their strong electrostatic interactions with anionic moieties[43]. The extraction of 195.8 mAh g^{-1} from $Mg_2Mn(BO_3)_2$ cycled at 55°C can be seen in green in Fig. 2a, in addition to the significantly enhanced capacity, a sloping feature below 3.6 V is observed.

Polyanion electrodes are known to be more ionically insulating than layered metal oxides, with previous studies demonstrating that ball milling can significantly enhance capacity[23]. By reducing the particle size through ball milling, the surface area is increased, exposing more electrochemically active sites, while simultaneously shortening the ion diffusion pathways, facilitating the reversible (de)insertion of ions. Thus, $Mg_2Mn(BO_3)_2$ polycrystalline powders were ball milled for 30 minutes in an inert Ar atmosphere using a planetary ball mill. Scanning electron microscopy (SEM) and synchrotron X-ray diffraction (SXRD) confirmed a reduction in particle size from an average of 10 μm to 5

μm post-milling (see SI section S4). The ball-milled (BM) cathodes, when cycled at 55°C, demonstrated further improvements in capacity as seen in black in Fig. 2a. Notably, ball milling extended the range of the chemical process associated with the 3.6 V plateau. In hand-ground samples, this plateau spanned less than 30 mAh g^{-1}, whereas, in the ball-milled materials, this range was extended to approximately 60 mAh g^{-1} (equivalent to 0.25 mol of Mg removed per formula unit).

The promising capacity achieved by the BM $Mg_2Mn(BO_3)_2$ cathode during the first charge, alongside the extension of voltage plateaus, suggests the material's potential as a viable cathode candidate for Mg-ion batteries. Four distinct stages of the first charge-discharge cycle in the BM $Mg_2Mn(BO_3)_2$ were identified; uncharged cathode samples (blue), samples charged up to 3.6 V (purple), fully charged to 4.6 V (pink) and discharged down to 1.5 V after the first charge (grey), Fig. 2b. These underwent post-cycling analysis to investigate whether the observed capacity could be attributed to Mg-ion de-intercalation and transition metal redox in the $Mg_2Mn(BO_3)_2$ cathode structure.

2.2 Post-cycling Analysis

Ex-situ SXRD was conducted at the four key stages during cycling (Fig. 3a). Rietveld refinements of the diffraction data indicated no significant change in the unit cell volume across these states (see SI section S2 for refinement details). This lack of volumetric change aligns with the known stability of polyanion frameworks, which typically exhibit minimal structural distortions during ion (de)insertion as observed in earlier studies[44–46]. As such, the absence of volume changes in the unit cell after the first cycle does not rule out the occurrence of de-magnesiation.

To further probe the possibility of Mg extraction, *operando* X-ray absorption near-edge structure (XANES) spectroscopy was employed. This technique was used to indirectly investigate the possibility of de-magnesiation, by probing changes in the oxida-
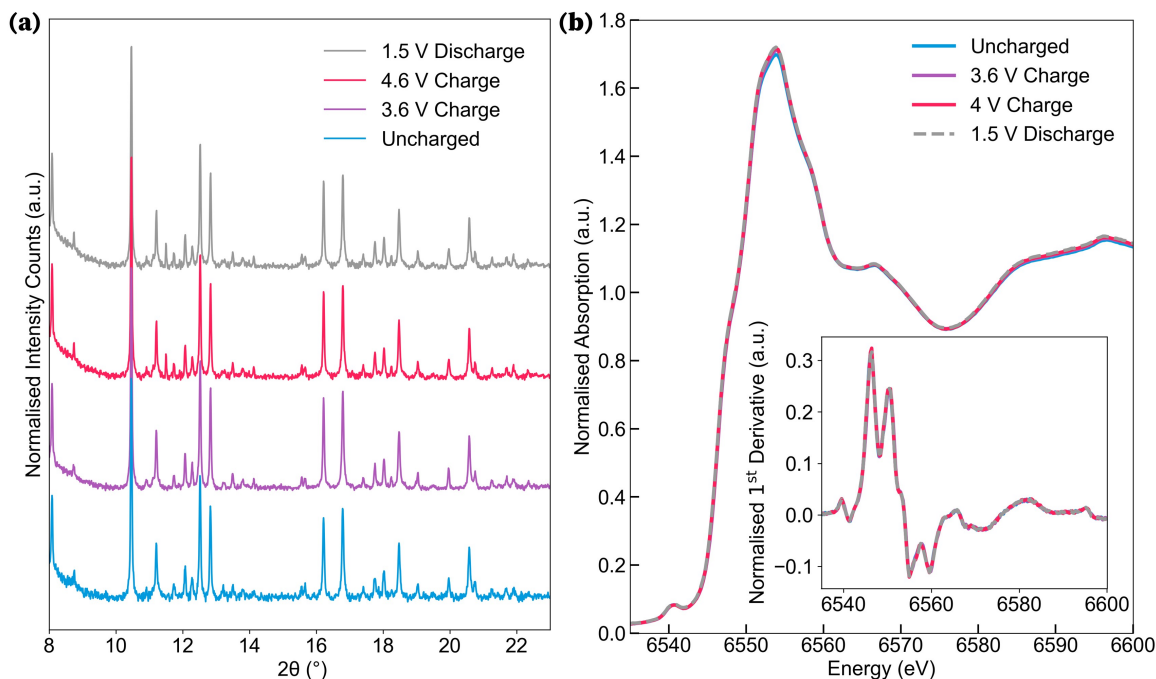
Fig. 3 (a) Normalised SXRD patterns and (b) normalised Mn K-edge *operando* XANES spectra of BM $Mg_2Mn(BO_3)_2$ cathode collected at various states of charge; uncharged (blue), post 3.6 V plateau (purple), end of charge at 4 V (pink), charged and discharged to 1.5 V (grey). (Inset) derivative of corresponding XANES spectra.

tion state of Mn during charge. $Mg_2Mn(BO_3)_2$ *operando* cells were cycled at room temperature at charge rates of C/20, with XANES data collected at the Mn K-edge (Fig. 3b). For all states of charge, the spectral data revealed minimal changes in the Mn K-edge XANES profiles. In particular, a shift in the edge position would be expected with a change in the oxidation state of Mn[47]. As shown in the derivative plot inset, the energy position of the absorption edge remains stationary, indicating that de-magnesiation from the cathode structure, accompanied by Mn oxidation, is not the source of the observed first-charge capacity.

Energy-dispersive X-ray spectroscopy (EDS) mapping was performed on *ex-situ* cycled cathode samples to assess changes in Mg

content at the particle surface, Fig. 4. A comparison of pristine BM $Mg_2Mn(BO_3)_2$ particles with ones charged to 4.6 V showed that the Mg:Mn ratio increased from 2.04(15):1 to 2.23(12):1 upon charging. This finding supports the hypothesis that Mg removal from the surface is unlikely, with the possibility that a minor amount of manganese dissolution into the electrolyte may occur. Transition metal dissolution is a well-documented phenomenon in TM oxide cathodes, with Mn known to be particularly prone to doing so[48-50].

The case study presented above on the ball-milled *orthoborate* system $Mg_2Mn(BO_3)_2$ demonstrates that despite the large capacity reached on the first charge, magnesium deintercalation from
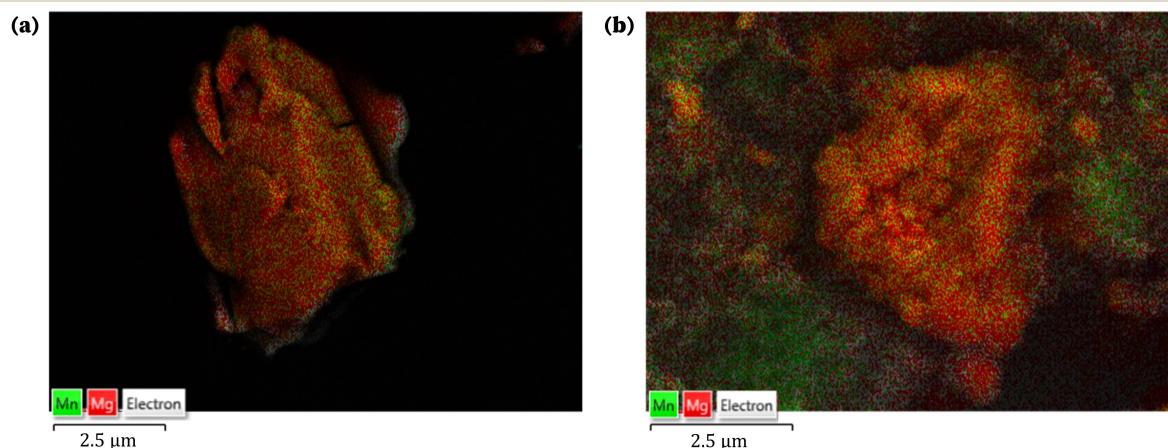

Fig. 4 Secondary electron SEM image with overlay of EDS maps for (a) BM $Mg_2Mn(BO_3)_2$ uncharged cathode material and (b) charged to 4.6 V. Here the green colour-map represents Mn and the red represents Mg.
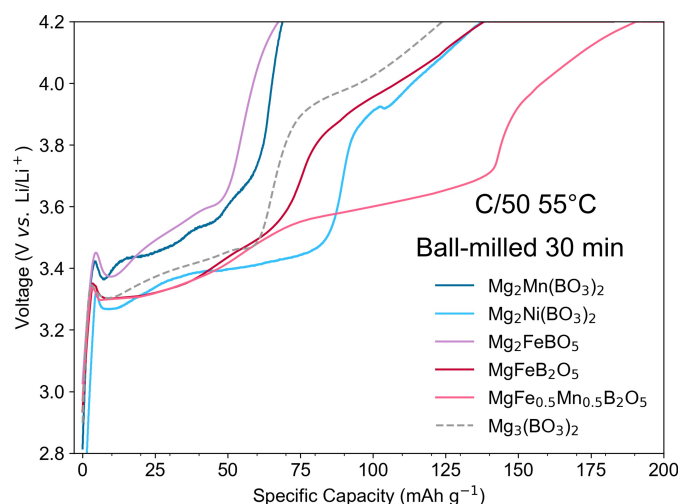
Fig. 5 Electrochemical profiles of ball-milled borates charged to 4.6 V at a rate of C/50 at 55°C, followed by a voltage hold at 4.6 V until the current decayed to C/200. This figure focuses on the similar voltage plateau between 3.3–3.5 V for district borate groups and transition metals (Fe, Mn and Ni), with full electrochemical data shown in Fig. S9.

the bulk cathode phase is not occurring.

3 Behaviour of Other Borate Polyanions

3.1 Electrochemical Inactivity of Crystalline Phase

Each borate was synthesised in phase pure form, ball milled and cycled vs Li metal anode in LP30 electrolyte at 55°C, following the optimised procedure developed for $Mg_2Mn(BO_3)_2$. The first charge electrochemical behaviour of the borates can be seen in Fig. 5, and the full first cycle charge-discharge curves are individually shown in Fig. S9. In a similar manner to $Mg_2Mn(BO_3)_2$, each cathode exhibited promising first-charge capacities (>130 mAh g^{-1}), with compounds behaving similarly independently of the TM (Fe, Mn or Ni). XANES, SEM-EDS and SXRD analyses conducted at various states of charge (SI sections S7, S12 and S3, respectively) confirm that, for all the borates studied, the observed first-charge capacities are not accompanied by bulk structural changes, transition metal oxidation, or de-magnesiation.

3.2 Similar Electrochemical Behaviour

Despite the verified lack of de-magnesiation, the borates in this study demonstrate promising first-charge capacities. Additionally, the initial charge profiles for all materials exhibit a common fea-ture: a plateau appearing between 3.2-3.6 V, hereafter termed the 'first charge plateau' (Fig. 5). This behaviour is observed irrespective of the specific TM or polyanion group involved, a finding which is unexpected given that the varying TMs (Fe, Mn and Ni) would typically result in different half-cell potentials for de-magnesiation. We also note that this plateau differs from the lower-potential feature (<3 V) observed in $MgFeB_2O_5$ samples containing significant Fe metal impurities, which we ascribed to the oxidation of Fe(0) [41].

To investigate this phenomenon further, $Mg_3(BO_3)_2$, which lacks redox-active ions, was synthesised, ball milled, and cycled vs Li metal following the same protocol. Despite the lack of TMs in $Mg_3(BO_3)_2$, we observe a similar capacity and voltage profile (Fig. 5), suggesting that this common feature in the first-charge capacity involves neither TM dissolution nor TM redox activity.

These observations suggest that a shared electrochemical process underpins the first-charge behaviour across the borate polyanions. A further effort was put into identifying the possible origin of this first charge capacity common to the borate polyanion systems studied in this work.

3.3 Amorphous Surface Layer

SXRD studies of the cathode materials confirm that the capacity does not arise from any crystalline impurities, in contrast to our previous study of non-phase-pure $MgFeB_2O_5$ [41]. The common presence of the first-charge plateau in non-BM cathode materials cycled at 55°C (Fig. 2a), which becomes more pronounced upon ball milling, suggests that the electrochemical process involves a surface component already present in the as-synthesised materials. The increase in surface area induced by ball milling is likely to enhance the contribution of this surface component to the overall capacity.

High-resolution transmission electron microscopy (HR-TEM) was utilised to image the amorphous surface layer; however, results were inconclusive. Although evidence of an amorphous layer was observed (Fig. S14), the sensitivity of the cathode surface to beam exposure (Fig. S15), combined with the polycrystallinity of the bulk cathode materials, complicated the interpretation of the data.

We therefore shifted the investigation to determining the chemical composition of the possibly electrochemically active surface by performing X-ray photoelectron spectroscopy (XPS) on as-synthesised (non-BM) materials. Elemental quantification from

Table 2 Elemental quantification obtained from XPS Survey spectra, collected for the pristine (non-BM) borate polyanions in this study. Clearly illustrating the non-stoichiometric surface composition, with the excess boron and carbon. Based on the XPS penetration depth, this is assumed to represent the atomic composition of the top ≈10 nm of the particle surface. Here, the TM row can correspond to a combination of Fe 2p$_{3/2}$, Mn 2p$_{3/2}$ and Ni 2p based on the chemical composition of each polyanion.

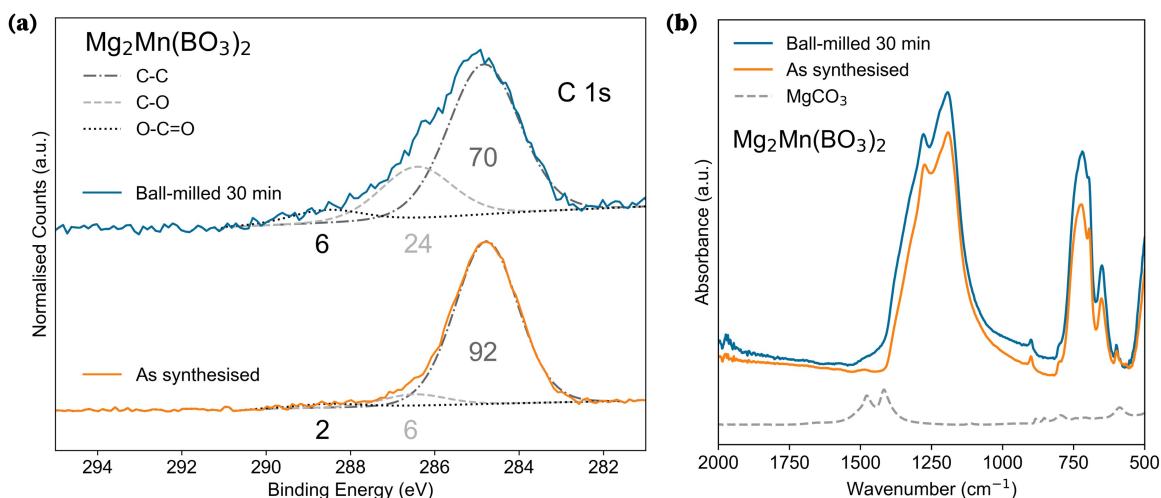| Element	$MgFeB_2O_5$ At%	$MgFe_{0.5}Mn_{0.5}B_2O_5$ At%	$Mg_3(BO_3)_2$ At%	$Mg_2Ni(BO_3)_2$ At%	$Mg_2Mn(BO_3)_2$ At%
O (1s)	44.4	39.0	55.7	54.9	55.3
C (1s)	25.3	35.3	13.4	18.1	15.2
B (1s)	25.2	20.4	22.9	20.5	18.6
Mg (1s)	1.4	1.6	7.9	4.0	4.9
TM (2p)	3.8	3.7	–	2.5	6.0

Fig. 6 Comparison of (orange) as-synthesised and (blue) ball-milled *orthoborate* $Mg_2Mn(BO_3)_2$ particles. (a) XPS C 1s, showing the presence of surface carbonates, the numbers in grey correspond to the relative percentage of each fit component to the C 1s spectra, full details can be found in Table S8. (b) FTIR Spectra, where the region between 1500-1400 cm^{-1}, seen to increase with ball milling, is characteristic of C-O bonds, as evidenced by the $MgCO_3$ spectra (grey-dashed) placed as a reference (not to scale).

the XPS survey scans is summarised in Table 2. This revealed that the first ≈ 10 nm of surface depth consisted of boron, carbon, and oxygen, with minimal Mg or TMs detected. The values in Table 2 can be used to estimate the excess boron present on the surface of the particle, with $\approx 15 - 20$ At% in excess of the expected stoichiometric ratios (full calculation in SI section S10). The presence of excess boron cannot be attributed to environmental reactions and is therefore considered direct evidence of an amorphous surface layer on the particles. Furthermore, the observed boron-to-oxygen ratio suggests that this surface layer may be composed of B_2O_3. This composition is well-documented to form glassy phases in natural systems, which are known to be thermodynamically stable[51–53]. Beyond this, significant amounts of carbon are detected on the surface. The Carbon 1s spectra show that the C environments in the as-synthesised samples contain C-O bonds associated with the presence of carbonate species, as exemplified in Fig. 6a for as-synthesised $Mg_2Mn(BO_3)_2$ (orange). These XPS results suggest the presence of a carbon- and boron-rich amorphous layer over the crystalline cathode surface, undetectable by SXRD, which may contribute to the first-charge capacity.

An XPS study on the changes in particle surface as a function of ball-milling time was conducted on *orthoborates* $Mg_2Ni(BO_3)_2$ and $Mg_2Mn(BO_3)_2$. No significant changes in the elemental composition or transition metal oxidation of the *orthoborates* were observed compared to as-synthesised samples, even with extended 6-hour ball milling of $Mg_2Ni(BO_3)_2$ (Section S10). The key result from this investigation is highlighted in Fig. 6a, where the C 1s spectra of $Mg_2Mn(BO_3)_2$ show the marked increase with ball milling of C-O (286.4 eV) and O-C=O (288.6 eV) bonds, as compared to the C-C (284.8 eV) bonds.

Fourier Transform Infrared (FT-IR) spectroscopy was employed to further examine the effects of ball milling (Section S9). A comparison of FT-IR spectra for $Mg_2Mn(BO_3)_2$ before and after ball milling is presented in Fig. 6b. The spectra reveal an increased

shoulder at 1500–1400 cm^{-1}, which corresponds to asymmetric v_3 CO_3^{2-} vibrations[54–57]. This observation qualitatively supports the results observed in XPS and suggests an increase in the fraction of C-O bonds (increase in carbonates) on the amorphous surface layer. Fig. 7 shows the C 1s spectra of all the BM polyanion materials cycled in this work; it is clear that the carbonate bonds are a common surface characteristic across all borates.

Ex-situ XPS was performed on charged cathode samples of *orthoborates* $Mg_2Mn(BO_3)_2$ and $Mg_3(BO_3)_2$, as well as *pyroborate* $MgFeB_2O_5$, to track changes in the surface amorphous layer following the first charge. However, identifying specific chemical changes on the surface of our borate particles from the XPS spectra proved challenging. The key spectra, which were important for tracking the reactions of the amorphous surface, namely the B 1s and C 1s, became difficult to analyse. The C 1s spectra increased in complexity, with additional C environments coming from the conductive carbon, binder and electrolyte residues present at the particle surface at the end of the first charge, making it difficult to isolate the cathode-specific components (Fig. S24 a-c). The B 1s analysis is hindered by the overlap with P 2s peaks, where the P is introduced from the electrolyte salt (Fig. S25 a-c).

Despite these challenges, some general trends are observed for all three charged borates analysed with XPS (full discussion in SI section S10). The O 1s spectra exhibited similar changes for all samples upon charging, with the appearance on charge of a second fit component (534 eV) for $Mg_3(BO_3)_2$ and $MgFeB_2O_5$, and an increase in % contribution from the same fit component for $Mg_2Mn(BO_3)_2$ (Fig. S25 d-f). Additionally, the surface of the samples after charging showed significant variations in the Mg 1s spectra (Fig. S23 and S24 d-f), with an increase in the fit contribution of the 1305 eV peak across all samples. The changes occurring in the O and Mg 1s spectra suggest modifications in the local surface environments, supporting the hypothesis that the amorphous layer undergoes chemical changes during the first
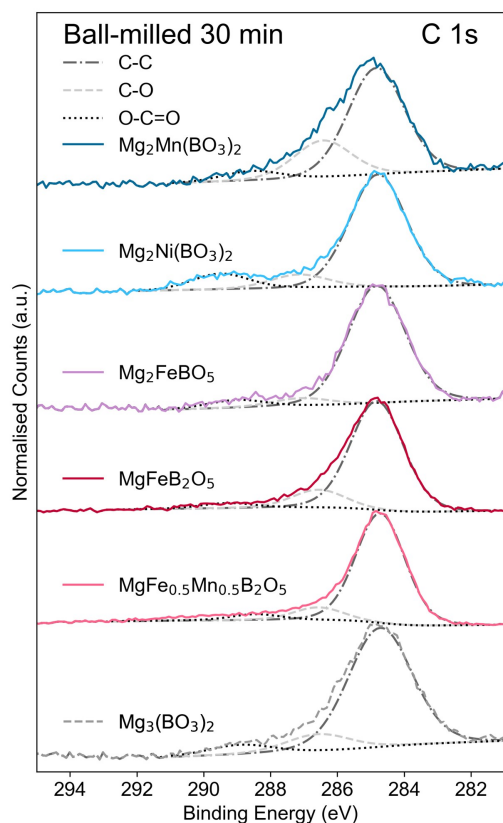
Fig. 7 (a) XPS C 1s Spectra of the cathode materials investigated in this work, showing the presence of surface carbonates (SI Table S8)

charge. However, due to the complexity of the surface and the unique chemical environments of each borate material, assigning specific bonding environments to XPS peaks was not possible, and no universal reaction mechanism could be identified.

To assess whether the carbonates identified via XPS and FT-IR contribute to the electrochemical activity, online electrochemical mass spectrometry (OEMS) was conducted on ball-milled *orthoborate* $Mg_2Ni(BO_3)_2$, Fig. 8. Upon charging above 3.3 V, H_2 evolution was detected at the onset of the first charge plateau, which is attributed to the reduction at the anode of protons originating from the cathode; these protons could arise from a combination of surface physisorbed H_2O, chemisorbed protons or H_2O in the amorphous layer, released as part of an oxidation reaction involving the amorphous surface layer or electrolyte reactions with the metastable surface layer. The total H_2 evolved over this plateau corresponds to 0.867 μmol. Assuming a 2 e$^-$/H_2 reduction reaction (see SI for the relevant calculations), this would only account for 11.56 mAh g^{-1} ($\approx 29.5\%$) of the capacity observed below 3.6 V (39.19 mAh g^{-1}). Thus there must be another electrochemical reaction that accompanies the proton/water release at the cathode. Subsequent thermogravimetric analysis coupled with mass spectrometry (TGA-MS) results showed no significant water loss from the cathode material until the onset of the PVDF decomposition reaction (SI section S14), discounting physisorbed water as the likely protic source. Thus, the origin and underlying mechanisms for H_2 evolution below 3.6 V remain unclear, and a more

detailed investigation of this phenomenon is necessary.

Above 3.6 V both CO_2 and H_2 were released. The release of CO_2 can be attributed to the electrochemical oxidation of surface carbonates. CO_2 release reactions have been shown to induce further knock-on degradation processes in other systems [58–60]. The further H_2 release observed above 3.6 V may be related to the CO_2 release.

The total amount of CO_2 and H_2 detected by OEMS amounted to 0.185 μmol and 0.837 μmol respectively, which would account for 26.3% of the capacity above 3.6 V (53.13 mAh g^{-1}), assuming a 2 e$^-$/CO_2 and 2 e$^-$/H_2 stoichiometries (equations in SI section S13) [61]. The capacity measured above 3.6 V is, at least in part, attributable to parasitic reactions associated with the evolution of CO_2, which are likely linked to the decomposition of surface carbonate species (and possibly coupled electrolyte degradation processes). Consequently, such capacity contributions should not be directly interpreted as arising from Mg deintercalation from the active cathode phase, as has occasionally been assumed in prior studies on novel RMB cathode materials.

4   Discussion

The main scope of this study was to evaluate the possibility of demagnesiation from borate polyanions. We have concluded that the crystalline bulk of the borates is electrochemically inactive under the conditions used in this work. This finding is particularly significant given the chemical diversity of the three borate classes examined, as summarised in Table 1.

In most polyanionic systems, electrochemical activity is known to depend on the structural polymorph present. For instance, a sodium polyanion analogous to the borate systems studied here $NaFePO_4$, crystallizes in either the *maricite* or *triphylite* polymorphs [62], with the former electrochemically inactive and the latter active [63,64]. For *triphylite* polymorphs, activity is attributed to the connectivity of the polyanion groups and the presence of Na diffusion channels, which are absent in the *maricite* phase [63,65].

In contrast to the *maricite* $NaFePO_4$ example, in this work we investigate three distinct classes of borate materials with varying structures, metal site configurations, and polyanion connectivities. This systematic study demonstrates that the lack of Mg mobility in these borates is not solely dictated by specific polyanion connectivity or the presence of ionic diffusion pathways, as seen in $NaFePO_4$, but rather represents a more general phenomenon in this class of materials.

Beyond this result, further effort was employed to decipher the origin of the high capacities seen in the first charge and common to all the borate cathode materials. A combination of analytical techniques was employed in an attempt to detect the presence and track the changes of an amorphous layer on the surface of our particles, believed to be the source of the potentially promising capacity. Due to the very thin nature of this surface layer, its low volume contribution compared to the crystalline bulk of the particles, its sensitivity to beam exposure (in an electron microscope) and its amorphous nature, efforts to study it proved challenging. Nonetheless, XPS analysis revealed a $\approx 15-20$ At% excess of B at all borate surfaces, which cannot be attributed to atmospheric contamination. This was regarded as evidence for
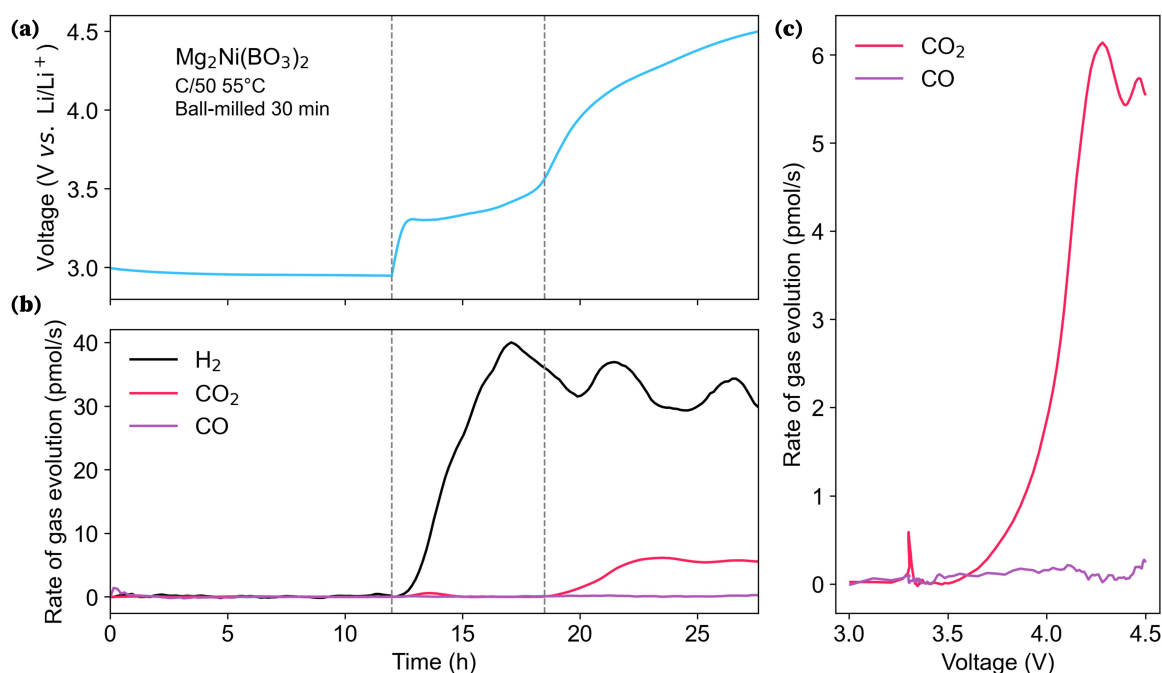
Fig. 8 OEMS data of ball-milled *orthoborate* $Mg_2Ni(BO_3)_2$ (a-b) showing evolution of H_2, CO_2 and CO corresponding to m/z= 2, 44 and 28, respectively (a) as a function of time, with the cell voltage trace shown in (a). (c) Evolution of CO_2 and CO during the charging process plotted *vs.* voltage.

the presence of a boron-rich amorphous layer approximately 10 nm in thickness at the particle surface.

In support of this observation, we underline that the solid-state synthesis approach employed in this work proceeded *via* crystallisation from an intermediate borate melt phase. Pure anhydrous B_2O_3 is known to form a melt phase at low-temperatures[66] and not crystallise under ambient pressure conditions[51–53]. It is therefore widely recognised as an excellent glass former, and due to its high solubility and low viscosity, forms a broad range of stable glasses when combined with other oxides[67]. These characteristics make it highly plausible that a residual amorphous borate layer persists on the particle surfaces after the final crystallisation synthesis steps. Supporting this hypothesis, a recent XPS study on $Mg_2B_2O_5$ nanorods also reported a non-stoichiometric, amorphous surface layer on the borate material[68], corroborating our conclusion that an amorphous phase forms during the synthesis of this class of materials.

Given the presence of this surface layer, we suggest that the capacity-enhancing effect of ball milling can be attributed to two main mechanisms: i) the observed increase in carbonates on the particle surface after ball milling and ii) an increase in the amorphous surface area exposed to the electrolyte. Since XPS analysis revealed no significant changes in the elemental composition following ball milling, we propose that the crystalline surfaces exposed upon particle fracture undergo further amorphisation during the milling process, likely driven by the high localised temperatures reached in the process.

We further rule out that the capacity-enhancing effect of ball milling is purely capacitive, as electrochemical profiles of ball-milled samples at room temperature exhibited poor capacities of

less than 30 mAh g^{-1}, on the same order as non-ball-milled samples, Fig S38. Furthermore, online electrochemical mass spectrometry (OEMS) indicates that the at least some of the capacity above 3.6 V can be associated with gas-producing reactions.

Recent studies have demonstrated that surface layer reactions and ball milling can induce significant capacity in cathode materials otherwise considered electrochemically inactive. Berlanga *et al.* showed that ball milling *maricite* $NaFePO_4$ led to the formation of an electrochemically active amorphous surface layer, which accounted for the majority of the reversible capacity beyond the first charge[69], a finding that strongly parallels the behaviour observed in our borate systems. Similarly, Xu *et al.* attributed the enhanced capacity of ball-milled Li_2MnO_3 to the formation of surface Li_2CO_3, with decomposition of this carbonate layer contributing significantly to the first-charge capacity[70]. While amorphous Li_2CO_3 surface layers have previously been reported to form via exposure to ambient air or moisture[71–73], such pathways are unlikely in our case as all synthesis steps were conducted under flowing Ar, and subsequent storage, handling and ball milling were performed under an inert Ar atmosphere. Instead, we propose that the majority of carbon surface species originate from carbon-containing TM oxalate used during the melt-phase synthesis.

Taken together, our XPS, OEMS, and FT-IR analyses, along with the supporting literature, indicate that the high irreversible capacity observed in these polyanion materials arises from a combination of carbonate degradation and side reactions mediated by a disordered, electrochemically active borate-rich surface layer. Due to the thin and amorphous nature of this layer, efforts to conclusively identify an electrochemical reaction mechanism proved

inconclusive; nonetheless, through OEMS, we have demonstrated that the capacity above 3.6 V is associated with parasitic reactions evolving H_2 and CO_2 indicating the possible degradation of surface carbonates, some containing bound water.

The capacity observed below 3.6 V is also associated with H_2 evolution, although this alone accounts for only a small fraction of the capacity ($\approx$ 12.5% for ball-milled *orthoborate* $Mg_2Ni(BO_3)_2$. The hydrogen evolution observed with the onset of the plateau is attributed to proton release from the cathode and hints at an electrochemical process involving the particle surface. Borate glasses have been studied for a wide variety of applications[74,75] and shown to take part in electrochemical conversion reactions[35,75,76] exhibiting good ionic conductivities[77]. Thus, the possibility of a surface-mediated reaction involving a conversion of the amorphous borate layer, and its reaction with the electrolyte, could plausibly contribute to the first charge capacity below 3.6 V. Importantly, the combined capacity calculated from the evolved H_2 and CO_2 only accounts for $\approx$ 27.22% of the observed first charge capacity, indicating the presence of significant additional surface-mediated reactions, the nature of which remains to be investigated.

Crucially, in none of the above-mentioned experimental investigations did we observe demagnesiation from the cathode material surface, underlining that the promising capacity cannot be attributed to demagnesiation of the bulk nor the surface layer.

Finally, the role of corrosion, electrolyte decomposition and surface degradation should not be overlooked in these systems, given the high operational temperatures and voltages of the cells[48]. We suggest a combination of the above-mentioned processes to be the most likely source of the high capacities and the common first-charge plateau observed across all the polyanions in this work.

5 Conclusions

Five cathode compositions from three chemically and structurally distinct borate polyanion groups - $Mg_2M(BO_3)_2$ ($M=$ Ni, Mn), $MgMB_2O_5$ ($M=$ Fe, $Mn_{0.5}Fe_{0.5}$), and Mg_2FeBO_5 - were studied as candidate cathode materials for high voltage rechargeable Mg-ion batteries. At room temperature, less than 15 % of the theoretical capacity was achieved. For ball-milled samples cycled at 55 °C, despite the large capacities on first charge and promising electrochemistry, XANES and SXRD studies revealed magnesium deintercalation was not occurring. Together, these results showed that under the tested conditions, none of the investigated magnesium polyanions showed promise as Mg (de)intercalation cathodes.

These findings have broad implications, indicating that the lack of de-magnesiation in these materials is not solely attributed to the absence of viable diffusion pathways or structural connectivity within a single borate composition. Instead, this suggests a more fundamental limitation which could apply to borate polyanions as a whole; the insulating nature of the polyanion systems, the presence of highly ionic oxygen and the one-dimensional channels for (de)intercalation, seem to be a barrier to Mg mobility and diffusion out of the crystal structure. Although unlikely, the authors do not wish to exclude the possibility that different synthesis procedures, nanosizing, alternate electrolyte selections, or

surface coatings could positively affect the Mg mobility in these materials.

Beyond this result, significant effort was devoted to understanding the origin of the promising first-charge capacities, marked by a common feature across all borate polyanion cathodes: a substantial, irreversible capacity arising from a plateau below 3.6 V. This is likely linked to gas evolving reactions involving an amorphous layer of approximately 10 nm thickness at the surface of the particles. This work suggests a potential novel source of capacity that could arise in a wide class of borate materials. Importantly, this study contributes to the narrative of the effects of surface reactions and ball milling in increasing the capacity of electrochemically inactive cathode materials[69,78]. As with the previous studies in the literature, we underline the need to better understand surface amorphisation and instabilities caused by ball milling, which could give rise to the observed capacities.

Finally, this comprehensive study highlights a broader challenge across multivalent systems: electrochemical capacity and structural evolution alone are insufficient indicators of reversible ion intercalation. As highlighted by Johnson *et al.*, ambiguities in the Mg battery literature often stem from inadequate characterisation protocols, which typically rely solely on these metrics[79]. Mg's divalent nature introduces significant kinetic barriers, and promising electrochemical profiles can arise from competing processes involving side reactions rather than true Mg (de)intercalation, as exemplified in this work. These insights extend beyond Mg batteries to all multivalent ion battery systems. Given that multivalent ion battery chemistry is far less developed than its Li-ion counterpart, we emphasise the importance of rigorous and standardised post-cycling protocols for advancing these technologies. Our work underscores the complexity of cathode material behaviour in RMBs and highlights the critical role of comprehensive post-cycling characterisation in unravelling these mechanisms and understanding Mg deintercalation in novel compounds.

6 Experimental

All cathode materials were produced via solid-state synthesis. Powdered reactants were weighed in stoichiometric amounts and hand-ground with a mortar and pestle, and subsequently mechanically ball-milled before being pressed into a 13 mm diameter pellet. The ground and pelletised mixtures were placed in alumina crucibles and slowly heated ($\leq$ 3°C/min) to high temperatures in a resistance tube furnace under flowing Ar. Cu foils were added in the tube furnace to minimise reaction of the materials with trace amounts of oxygen and stabilise the transition metals. Due to the difficulty in synthesising these materials, multiple heating steps were necessary to obtain the desired purity and crystallinity. A summary of the steps and precursors used to synthesise each material can be found in the SI.

A 30-minute ball-milling procedure was performed on all the as-synthesised cathode materials. A Fritsch Pulverisette 6' planetary mono mill was used. $\approx$ 200 mg of cathode samples were mixed in a 1:10 mass ratio with 3 mm zirconium dioxide balls and placed in a ball-milling container, which was sealed in an Ar glovebox and then transferred to the machine. The powders

were milled at 550 rpm for 30 minutes (5 minutes on, 5 minutes off, 6 repetitions to avoid overheating). The container was then returned to the glovebox, where the ball-milled material was retrieved and stored.

Synchrotron Powder X-ray Diffraction (SXRD) was collected on samples at the Diamond Light Source I11 beamline ($\lambda = 0.824110$ Å) using the Mython-2 position-sensitive detector at room temperature. Samples were packed into a 0.5 mm diameter capillary and sealed with Araldite Adhesive Bicomponent epoxy under a controlled Ar atmosphere. TOPAS v5[80] was used to perform Rietveld Refinement[81] on the resulting SXRD data over a 2θ range of 10-80°. The peak shapes for Rietveld analysis were modelled using a pseudo-Voigt function[82], and the background was modelled using a Chebyshev polynomial with 17 terms.

After phase purity was confirmed, CR2032 coin cells were constructed to measure electrochemical performance. From the point of synthesis onwards, all cathode materials were stored and handled in an Ar atmosphere for cell assembly, cycling, and post-cycling analysis to minimise contamination and degradation. Cathodes were prepared by grinding the borates using a mortar and pestle for 10 minutes with Ketjen Black Carbon and PVDF binder (Kynar Flex® 2801-00) in a 60:30:10 mass ratio. Each cell used 5-6 mg of powder placed on the coin cell base, combined with a Whatman glass fibre separator (GF/B 55 mm diameter) soaked in 120 μL of LP30 electrolyte (Sigma-Aldrich) (1 M LiPF$_6$ in 50/50 v/v ethylene carbonate and dimethyl carbonate, EC/DMC) vs Li metal anode. A Belleville spring provided the necessary pressure in the cell. The spacers, springs, and casings were grade 316 stainless steel.

Electrochemical testing was performed by galvanostatic cycling on a Landt CT3001A device between 1.5 V and 4.6 V. Before charging, cells were rested for 6 hours while the open circuit voltage was measured. A charge rate of C/50 and constant oven temperature of (55°C) were used to enhance notoriously slow Mg ion diffusion. Once cycled, *ex-situ* cathode samples were obtained by disassembling coin cells in an Ar atmosphere glovebox and washing collected powders in DMC to remove residual electrolyte and salts.

Mn and Fe K-edge X-ray Absorption Near Edge Spectroscopy (XANES) spectra were collected at the B18 beamline[83,84] of Diamond Light Source, UK. *Ex-situ* samples were prepared by hand milling extracted cathode samples with 10 mg of dried cellulose and pressing into 6 mm diameter pellets. *Operando* spectra for *orthoborate* Mg$_2$Mn(BO$_3$)$_2$ were collected using customised *operando* cells vs Li metal. An X-ray beam was vertically collimated using a Pt coated mirror before passing through the Si(111) double crystal monochromator. High-order harmonics in an incident beam were eliminated by using two dedicated Pt-coated mirrors operating at an 8 mrad incidence angle. Energy calibration was achieved by the simultaneous measurement of 5 μm-thick Fe, Ni or Mn metal foils for the corresponding absorption edges. In-house *operando* cells were cycled at a rate of C/20 at ambient temperature, and XANES spectra were intermittently recorded at 10-minute intervals in transmission mode using a quick extended X-ray absorption fine structure technique. The room-temperature *operando* cycling reproduced the electrochem-

ical behaviour observed in our laboratory-based coin cells, albeit reaching a reduced capacity than that achieved at 55°C, a phenomenon we attribute to the slower kinetics at lower operational temperatures, as seen in Fig. S10.

Ex-situ Scanning Electron Microscopy Energy Dispersive X-ray Spectroscopy (SEM-EDS) maps and spectra were acquired using an Oxford Instruments X-maxN 80 EDS system on a TESCAN MIRA3 FEG-SEM operated at 10 kV. Samples were transferred from the glovebox to the SEM chamber using an air-tight Kammrath and Weiss transfer module.

Fourier-transform infrared (FTIR) spectroscopy was performed on the pristine cathode materials directly in an Ar glovebox using an Agilent Technologies FTIR spectrometer (Cary 630) in the mid-IR range (3500–400 cm^{-1}).

A Thermo Scientific Talos F200X G2 operating at 200 kV was utilised for TEM analysis. TEM images were acquired using a Ceta 4k x 4k CMOS camera. The sample was prepared on a lacey carbon-coated 300 mesh Cu grid (EM Resolutions).

X-ray photoelectron spectroscopy analysis was performed using a Thermo Scientific Escalab 250Xi fitted with a monochromated Al kα X-ray source (1486.7 eV). All data were recorded with an X-ray beam size of 650 μm, a pass energy of 20 eV at a step size of 0.1 eV. Electronic charge neutralisation was achieved using an ion source. Ion gun current = 100 μA. Ion gun voltage = 40 V. All sample data were recorded at a pressure below 10^{-8} Torr and a room temperature of 294 K. Data were analysed using CasaXPS v2.3.26rev1.0N. Samples were transferred from the glovebox using an air-tight transfer holder to avoid exposure to air.

Online electrochemical mass spectrometry (OEMS) measurements were conducted using a Pfeifer Thermostar quadruple mass spectrometer in a continuous flow setup, which carries the evolved gas from the cell headspace to the spectrometer[60,85–87]. The OEMS cell consists of a coin cell (0.23 mm hole on the top case) housed inside a 1-inch Swagelok-type cell. The cell was assembled in a glovebox by dropping a mixture of active material, carbon and binder powder on a spacer against a Li metal chip with two layers of separator (polypropylene and glass fibre) and 100 μl of the LP30 electrolyte. It was then attached to the setup via quick connects, avoiding exposure to the air. The cell was charged to 4.5 V and discharged to 1.5 V at C/50 with rest periods before and after cycling at open circuit voltage (OCV) to ensure sufficient background and avoid any signal drift.

Conflicts of interest

The authors have no conflicts of interest to declare.

Data availability

Placeholder   Repository   for   Data: *https://www.repository.cam.ac.uk/handle/XXXX/XXXXXX*

Acknowledgements

Notes and references

1 G. E. Blomgren, *Journal of The Electrochemical Society*, 2017, **164**, A5019–5052.

2 R. Schmuch, R. Wagner, G. Hörpel, T. Placke and M. Winter, *Nature Energy*, 2018, **3**, 267–278.

3 S. Weitemeyer, D. Kleinhans, T. Vogt and C. Agert, *Renewable Energy*, 2015, **75**, 14–20.

4 I. E. Agency, *World Energy Investment 2020*, 2020, `https://iea.blob.core.windows.net/assets/ef8ffa01-9958-49f5-9b3b-7842e30f6177/WEI2020.pdf`, Accessed: 31-01-2025.

5 F. Europe, *Statistical Report 2022*, 2022, `https://www.fuelseurope.eu/publications/publications/statistical-report-2022`, Accessed: 31-01-2025.

6 H. Ambrose and A. Kendall, *Journal of Industrial Ecology*, 2020, **24**, 80–89.

7 M. Titirici, P. Johansson, M. C. Ribadeneyra, H. Au, A. Innocenti, S. Passerini, E. Petavratzi, P. Lusty, A. A. Tidblad, A. J. Naylor, R. Younesi, Y. A. Chart, J. Aspinall, M. Pasta, J. Orive, L. M. Babulal, M. Reynaud, K. G. Latham, T. Hosaka, S. Komaba, J. Bitenc, A. Ponrouch, H. Zhang, M. Armand, R. Kerr, P. C. Howlett, M. Forsyth, J. Brown, A. Grimaud, M. Vilkman, K. B. Dermenci, S. Mousavihashemi, M. Berecibar, J. E. Marshall, C. R. McElroy, E. Kendrick, T. Safdar, C. Huang, F. M. Zanotto, J. F. Troncoso, D. Z. Dominguez, M. Alabdali, U. Vijay, A. A. Franco, S. Pazhaniswamy, P. S. Grant, S. L. Guzman, M. Fehse, M. Galceran and N. Antuñano, *Journal of Physics: Energy*, 2024, **6**, 041502.

8 M. R. Palacin, P. Johansson, R. Dominko, B. Dlugatch, D. Aurbach, Z. Li, M. Fichtner, O. Lužanin, J. Bitenc, Z. Wei, C. Glaser, J. Janek, A. Fernández-Barquín, A. R. Mainar, O. Leonet, I. Urdampilleta, J. A. Blázquez, D. S. Tchitchekova, A. Ponrouch, P. Canepa, G. S. Gautam, R. S. R. G. Casilda, C. S. Martinez-Cisneros, N. U. Torres, A. Varez, J.-Y. Sanchez,

9 K. V. Kravchyk, M. V. Kovalenko, A. A. Teck, H. Shiel, I. E. L. Stephens, M. P. Ryan, E. Zemlyanushin, S. Dsoke, R. Grieco, N. Patil, R. Marcilla, X. Gao, C. J. Carmalt, G. He and M.-M. Titirici, *Journal of Physics: Energy*, 2024, **6**, 031501.

9 J. Bitenc and R. Dominko, *Frontiers in Chemistry*, 2018, **6**, 1–10.

10 R. C. Massé, C. Liu, Y. Li, L. Mai and G. Cao, *National Science Review*, 2021, **4**, 26–53.

11 D. Aurbach, Z. Lu, A. Schechter, Y. Gofer, H. Gizbar, R. Turgeman, Y. Cohen, M. Moshkovich and E. Levi, *Nature*, 2000, **407**, 724–7.

12 E. Levi, Y. Gofer, Y. Vestfreed, E. Lancry and D. Aurbach, *Chemistry of Materials*, 2002, **14**, 2767–2773.

13 E. Lancry, E. Levi, Y. Gofer, M. Levi, G. Salitra and D. Aurbach, *Chemistry of Materials*, 2004, **16**, 2832–2838.

14 L. F. Wan, B. R. Perdue, C. A. Apblett and D. Prendergast, *Chemistry of Materials*, 2015, **27**, 5932–5940.

15 M. Mao, T. Gao, S. Hou and C. Wang, *Chem. Soc. Rev.*, 2018, **47**, 8804–8841.

16 Z. Li, J. Häcker, M. Fichtner and Z. Zhao-Karger, *Advanced Energy Materials*, 2023, **13**, 2300682.

17 J. Muldoon, C. B. Bucur and T. Gregory, *Angewandte Chemie International Edition*, 2017, **56**, 12064–12084.

18 A. K. Padhi, K. S. Nanjundaswamy and J. B. Goodenough, *Journal of The Electrochemical Society*, 1997, **144**, 1188.

19 V. Legagneur, Y. An, A. Mosbah, R. Portal, A. Le Gal La Salle, A. Verbaere, D. Guyomard and Y. Piffard, *Solid State Ionics*, 2001, **139**, 37–46.

20 A. Yamada, N. Iwane, Y. Harada, S. Nishimura, Y. Koyama and I. Tanaka, *Advanced Materials*, 2010, **22**, 3583 – 3587.

21 P. Barpanda, D. Dwibedi and S. Ghosh, *Ionics*, 2015, **21**, 1801–1812.

22 C. Masquelier and L. Croguennec, *Chemical Reviews*, 2013, **113**, 6552–6591.

23 S. Awasthi, S. Moharana, V. Kumar, N. Wang, E. Chmanehpour, A. D. Sharma, S. K. Tiwari, V. Kumar and Y. K. Mishra, *Nano Materials Science*, 2024.

24 S.-H. Yang, H. Xue and S.-P. Guo, *Coordination Chemistry Reviews*, 2021, **427**, 213551.

25 G. D. D. Sanglay, J. S. Garcia, M. S. Palaganas, M. Sorolla, S. See, L. A. Limjuco and J. D. Ocon, *Molecules*, 2022, **27**, 8047.

26 Q. Ni, Y. Bai, F. Wu and C. Wu, *Advanced Science*, 2017, **4**, 1600275.

27 C. Christ and J. Clark, *Physics and Chemistry of Minerals*, 1977, **2**, 59–87.

28 H. Glass, *PhD thesis*, University of Cambridge, 2017.

29 D. V. D. Voort, J. M. E. de Rijk, R. van Doorn and G. Blasse, *Materials Chemistry and Physics*, 1992, **31**, 333–339.

30 J. J. Pryke, R. M. Kennard and S. A. Cussen, *Energy Reports*, 2022, **8**, 83–88.

31 H. Li, L. Wang, G. Cai, J. Fan, X. Fan and Z. Jin, *Journal of Alloys and Compounds*, 2013, **575**, 104–108.

32 J. Hriljac, R. Brown, A. Cheetham and L. Satek, *Journal of*

Solid State Chemistry, 1990, **84**, 289–298.

33 D. A. Perkins and J. P. Attfield, *J. Chem. Soc., Chem. Commun.*, 1991, 229–231.

34 P. Bordet and E. Suard, *Phys. Rev. B*, 2009, **79**, 144408.

35 J. Sottmann, L. Nataf, L. Chaix, V. Pralong and C. Martin, *The Journal of Physical Chemistry C*, 2018, **122**, 17042–17048.

36 Y. Takeuchi, *Acta Crystallographica*, 1952, **5**, 574–581.

37 R. Norrestam, K. Nielsen, I. Sotofte and N. Thorup, *Zeitschrift fur Kristallographie*, 1989, **189**, 33–41.

38 F. Strauss, G. Rousse, D. Alves Dalla Corte, M. Ben Hassine, M. Saubanère, M. Tang, H. Vezin, M. Courty, R. Dominko and J.-M. Tarascon, *Phys. Chem. Chem. Phys.*, 2016, **18**, 14960–14969.

39 S. H. Bo, C. P. Grey and P. G. Khalifah, *Chem. Mater.*, 2015, **27**, 4630–4639.

40 H. F. J. Glass, Z. Liu, P. M. Bayley, E. Suard, S.-H. Bo, P. G. Khalifah, C. P. Grey and S. E. Dutton, *Chemistry of Materials*, 2017, **29**, 3118–3125.

41 C. Tacconis, S. Dey, C. D. McLaughlin, M. T. Sougrati, C. A. O'Keefe, I. Mikulska, C. P. Grey and S. E. Dutton, *Chemistry of Materials*, 2025, **37**, 463–472.

42 E. M. Erickson, E. Markevich, G. Salitra, D. Sharon, D. Hirshberg, E. de la Llave, I. Shterenberg, A. Rosenman, A. Frimer and D. Aurbach, *Journal of The Electrochemical Society*, 2015, **162**, A2424.

43 E. Levi, M. D. Levi, O. Chasid and D. Aurbach, *Journal of Electroceramics*, 2009, **22**, 1573–8663.

44 Z. Gong and Y. Yang, *Energy Environ. Sci.*, 2011, **4**, 3223–3242.

45 A. K. Padhi, K. S. Nanjundaswamy and J. B. Goodenough, *Journal of The Electrochemical Society*, 1997, 1188–1194.

46 G. Chen, J. D. Wilcox and T. J. Richardson, *Electrochemical and Solid-State Letters*, 2008, **11**, A190.

47 K. R. Tallman, G. P. Wheeler, C. J. Kern, E. Stavitski, X. Tong, K. J. Takeuchi, A. C. Marschilok, D. C. Bock and E. S. Takeuchi, *The Journal of Physical Chemistry C*, 2021, **125**, 58–73.

48 Z. Ruff, C. Xu and C. P. Grey, *Journal of The Electrochemical Society*, 2021, **168**, 060518.

49 C. Zhan, T. Wu, J. Lu and K. Amine, *Energy Environ. Sci.*, 2018, **11**, 1730–1758.

50 S.-B. Son, Z. Zhang, J. Gim, C. S. Johnson, Y. Tsai, M. Kalensky, S. Lopykinski, O. Kahvecioglu, Z. Yang, A. T. Montoya and I. Bloom, *The Journal of Physical Chemistry C*, 2023, **127**, 1767–1775.

51 M. J. Aziz, E. Nygren, J. F. Hays and D. Turnbull, *Journal of Applied Physics*, 1985, **57**, 2233–2242.

52 A. C. Wright, *International Journal of Applied Glass Science*, 2015, **6**, 45–63.

53 V. Brazhkin, Y. Katayama, Y. Inamura *et al.*, *JETP Letters*, 2003, **78**, 393–397.

54 C. E. Weir and R. A. Schroeder, *Journal of Research of the National Bureau of Standards. Section A, Physics and Chemistry*, 1964, **68A**, 465–487.

55 S.-B. Choi, N.-W. Kim, D.-K. Lee and H. Yu, *Journal of*

56 S. Li, Z. J. Wang and T.-T. Chang, *PLOS ONE*, 2014, **9**, 1–13.

57 J. D. Rodriguez-Blanco, S. Shaw and L. G. Benning, *Nanoscale*, 2011, **3**, 265–271.

58 N. Mahne, S. E. Renfrew, B. D. McCloskey and S. A. Freunberger, *Angewandte Chemie International Edition*, 2018, **57**, 5529–5533.

59 B. L. D. Rinkel, D. S. Hall, I. Temprano and C. P. Grey, *Journal of the American Chemical Society*, 2020, **142**, 15058–15074.

60 Z. Lebens-Higgins, H. Chung, I. Temprano, M. Zuba, J. Wu, J. Rana, C. Mejia, M. A. Jones, L. Wang, C. P. Grey, Y. Du, W. Yang, Y. S. Meng and L. F. J. Piper, *Batteries & Supercaps*, 2021, **4**, 771–777.

61 D. Cao, C. Tan and Y. Chen, *Nature Communications*, 2022, **13**, 4908.

62 M. Avdeev, Z. Mohamed, C. D. Ling, J. Lu, M. Tamaru, A. Yamada and P. Barpanda, *Inorganic Chemistry*, 2013, **52**, 8685–8693.

63 P. Moreau, D. Guyomard, J. Gaubicher and F. Boucher, *Chemistry of Materials*, 2010, **22**, 4126–4128.

64 Y. Zhu, Y. Xu, Y. Liu, C. Luo and C. Wang, *Nanoscale*, 2013, **5**, 780–787.

65 M. Galceran, D. Saurel, B. Acebedo, V. V. Roddatis, E. Martin, T. Rojo and M. Casas-Cabanas, *Phys. Chem. Chem. Phys.*, 2014, **16**, 8837–8842.

66 D. Ehrt, *Physics and Chemistry of Glasses - European Journal of Glass Science and Technology Part B*, 2006, **47**, 669–674.

67 O. Akiko, B. Delia S and K. Toshihiro, *Phosphate and Borate Bioactive Glasses.*, Royal Society of Chemistry, 2022.

68 V. Singh, V. Pandey, V. K. Singh and M. R. Majhi, *Ceramics International*, 2023, **49**, 27086–27093.

69 C. Berlanga, M. T. Sougrati, A. J. Fernández-Ropero, N. Baaboura, N. E. Drewett, J. M. Lopez del Amo, G. Nolis, J. S. Garitaonandia, M. Reynaud, L. Stievano, M. Casas-Cabanas and M. Galceran, *J. Mater. Chem. A*, 2023, **11**, 20506–20517.

70 J. Xu, L. Kaufman, F. C. Robles Hernández, A. Pramanik, G. Babu, J. Nanda, B. D. McCloskey and P. M. Ajayan, *ACS Applied Energy Materials*, 2023, **6**, 5026–5036.

71 I. A. Shkrob, J. A. Gilbert, P. J. Phillips, R. Klie, R. T. Haasch, J. Bareño and D. P. Abraham, *Journal of The Electrochemical Society*, 2017, **164**, A1489.

72 A. Grenier, H. Liu, K. M. Wiaderek, Z. W. Lebens-Higgins, O. J. Borkiewicz, L. F. J. Piper, P. J. Chupas and K. W. Chapman, *Chemistry of Materials*, 2017, **29**, 7345–7352.

73 G. V. Zhuang, G. Chen, J. Shim, X. Song, P. N. Ross and T. J. Richardson, *Journal of Power Sources*, 2004, **134**, 293–297.

74 Y. Li, P. Li, X. Liu, Z. Jiang, Z. Shan, J. Zhang, S. Luo, Y. Yue and Y. Zhang, *Journal of Non-Crystalline Solids*, 2024, **637**, 123040.

75 W. Zhao, T. Xu, T. Li, Y. Wang, H. Liu, J. Feng, S. Ding, Z. Li and M. Wu, *Small*, 2018, **14**, 1802829.

76 A. Ibarra Palos, M. Morcrette and P. Strobel, *Journal of Solid State Electrochemistry*, 2002, **6**, 134–138.

77 C.-W. Wang, S.-J. Zhang, C. Lin, S. Xue, Y.-P. Deng, B. Zhang, L. Yang, X. Yao, L. Zeng, J.-T. Li, F. Pan and Z.-W. Yin, *Nano Energy*, 2023, **108**, 108192.

78 F. Xiong, Q. An, L. Xia, Y. Zhao, L. Mai, H. Tao and Y. Yue, *Nano Energy*, 2019, **57**, 608–615.

79 I. D. Johnson, B. J. Ingram and J. Cabana, *ACS Energy Letters*, 2021, **6**, 1892–1900.

80 A. A. Coelho, *Journal of Applied Crystallography*, 2018, **51**, 210–218.

81 H. M. Rietveld, *Journal of Applied Crystallography*, 1969, **2**, 65–71.

82 R. A. Young and D. B. Wiles, *Journal of Applied Crystallography*, 1982, **15**, 430–438.

83 S. Diaz-Moreno, M. Amboage, M. Basham, R. Boada, N. E. Bricknell, G. Cibin, T. M. Cobb, J. Filik, A. Freeman, K. Geraki, D. Gianolio, S. Hayama, K. Ignatyev, L. Keenan, I. Mikulska, J. F. W. Mosselmans, J. J. Mudd and S. A. Parry, *Journal of Synchrotron Radiation*, 2018, **25**, 998–1009.

84 A. J. Dent, G. Cibin, S. Ramos, S. A. Parry, D. Gianolio, A. D. Smith, S. M. Scott, L. Varandas, S. Patel, M. R. Pearson, L. Hudson, N. A. Krumpa, A. S. Marsch and P. E. Robbins, *Journal of Physics: Conference Series*, 2013, **430**, 012023.

85 I. Temprano, T. Liu, E. Petrucco, J. H. J. Ellison, G. Kim, E. Jónsson and C. P. Grey, *Joule*, 2020, **4**, 2501–2520.

86 W. M. Dose, W. Li, I. Temprano, C. A. O'Keefe, B. L. Mehdi, M. F. L. De Volder and C. P. Grey, *ACS Energy Letters*, 2022, **7**, 3524–3530.

87 W. M. Dose, I. Temprano, J. P. Allen, E. Björklund, C. A. O'Keefe, W. Li, B. L. Mehdi, R. S. Weatherup, M. F. L. De Volder and C. P. Grey, *ACS Applied Materials & Interfaces*, 2022, **14**, 13206–13222.

Prof. Siân Dutton

Professor in Physics and Solid State Chemistry,

Deputy Head of Department – Environment and Community

Director, Winton Programme for the Physics of Sustainability

Department of Physics

29 September 2025

Data Availability Statement

We confirm that all data for this article, including raw files for all the figures provided in the main manuscript and the supporting information will be available at **Apollo, the University of Cambridge institutional repository** (Apollo is CoreTrustSeal certified repository). The final DOI URL is: https://doi.org/10.17863/CAM.121628

Sincerely, on behalf of all the authors,

Siân E. Dutton